Sensitivity analysis of statistical measures for the reconstruction of microstructures based on the minimization of generalized least-square functionals

D. Balzani, D. Brands, J. Schröder, C. Carstensen

For the simulation of micro-heterogeneous materials the FE^2-method provides incorporation of the mechanical behavior at the microscale in a direct manner by taking into account a microscopic boundary value problem based on a representative volume element (RVE). A main problem of this approach is the high computational cost, when we have to deal with RVEs that are characterized by a complex geometry of the individual constituents. This leads to a large number of degrees of freedom and history variables at the microscale which needs a large amount of memory, not to mention the high computation time. Therefore, methods that reduce the complexity of such RVEs play an important role for efficient direct micro-macro transition procedures. In this contribution we focus on random matrix-inclusion microstructures and analyze several statistical measures with respect to their influence on the characterization of the inclusion phase morphology. For this purpose we apply the method proposed in Balzani and Schröder (2008); Balzani et al. (2009a), where an objective function is minimized which takes into account differences between statistical measures computed for the original binary image of a given real microstructure and a simplified statistically similar representative volume element (SSRVE). The analysis with respect to the capability of the resulting SSRVEs to reflect the mechanical response in some simple independent virtual experiments allows for an estimation of the importance of the investigated statistical measures.

1 Introduction

Many fields in metal processing like bending, deep-drawing or hydro-forming require a high ductility and stiffness of the used steel. According to advanced requirements in high-tech applications minimization of the dead weight by simultaneously increasing safety demands is one of the major goals in industry. In this context multi-phase steels have the potential to fulfill these requirements. This is due to the fact that the interplay between the individual constituents on the microscale yield outstanding strength and ductility properties. However, the complicated interactions of the individual phases of the micro-heterogeneous composite lead to complex local and global hardening effects and failures on the microscale. In order to capture these phenomena up to a certain accuracy we focus on a two-scale modeling approach. In this framework we attach a sufficient large section of the microstructure, approximated by a representative volume element (RVE), to each point of the macroscale. The numerical treatment of this approach is known as the direct micro-macro-transition procedure or the FE^2-method, see e.g. Smit et al. (1998), Brekelmans et al. (1998), Miehe et al. (1999), Schröder (2000), and Geers et al. (2003). Basic ideas for the direct micro-macro-transition approach with the application to dual-phase steels (DP-steels) are given in Schröder et al. (2008). The drawback of this approach is the high computational cost (high computation times), when we deal with large random microstructures. Furthermore, a large number of history variables occurs in this case which needs a large amount of memory. In order to circumvent these drawbacks we focus on the construction of statistically similar representative volume elements (SSRVEs) which are characterized by a much less pronounced complexity than the real random microstructures. The basic idea for this procedure is to find a simplified SSRVE, whose selected statistical measures are as close as possible to the real microstructure. The underlying minimization procedure is governed by least-square functionals, which compare the statistical measures of the real microstructure with the ones of the SSRVE. Beside the volume fraction we can use n-point probabilty functions, lineal-path functions, values of the specific internal surface and integral of mean curvature, etc. Parzen (1992) has shown that the two-point probability density function is correlated to the power spectral density in the frequency domain. Based on this work Povirk (1995) computed a simplified RVE for a composite consisting of a matrix with circular inclusions. In this generalized approach we describe the inclusion phase with splines and compare different statistical measures, in this context see Balzani and Schröder (2008); Balzani et al. (2009b).

2 Mechanical framework

In this work we focus on a direct micro-macro transition approach which takes into account a micromechanical boundary value problem for the determination of material properties at the macroscale. At the microscale an isotropic finite J_2-plasticity model with a von Mises yield law is taken into account for the response of the individual phases building up the microstructure.

2.1 Kinematics at different scales

Let $\mathcal{B} \subset \mathbb{R}^3$ denote a physical body at the microscale in its undeformed (reference) configuration at time $t = t_0$, parameterized in position vectors $\mathbf{X}$, wherein $\mathbb{R}^3$ is the euclidian three-dimensional space. A deformed (actual) configuration is denoted by $\mathcal{S} \subset \mathbb{R}^3$, parameterized by $\mathbf{x}$ at a fixed time $t \in \mathbb{R}_+$. Concentrating on the Boltzman continuum theory the deformation of the body can be interpreted as the motion of material points. The non-linear, continuous and one-to-one transformation $\boldsymbol{\varphi}(\mathbf{X}, t) : \mathcal{B} \rightarrow \mathcal{S}$ maps at time $t \in \mathbb{R}_+$ points $\mathbf{X} \in \mathcal{B}$ of the microscopic reference configuration onto points $\mathbf{x} \in \mathcal{S}$ of the actual microscopic configuration. For the description of deformations we define the microscopic deformation gradient

$$\mathbf{F}(\mathbf{X}) := \mathrm{Grad}[\boldsymbol{\varphi}_t(\mathbf{X})]. \tag{1}$$

At the macroscale we use the analogous definitions and use overlined characters to identify macroscopic quantities, then we consider the transformation map $\overline{\boldsymbol{\varphi}}(\overline{\mathbf{X}}, t) : \overline{\mathcal{B}} \rightarrow \overline{\mathcal{S}}$ with the macroscopic physical bodies $\overline{\mathcal{B}}$ and $\overline{\mathcal{S}}$ in the reference and in the actual configuration, respectively. Then, the macroscopic deformation gradient is defined by

$$\overline{\mathbf{F}}(\overline{\mathbf{X}}) := \mathrm{Grad}[\overline{\boldsymbol{\varphi}}_t(\overline{\mathbf{X}})]. \tag{2}$$

2.2 Constitutive modeling of the individual phases on the microscale

In order to solve the boundary value problem on the microscale, we have to set up constitutive equations for the individual phases on the microscale. During the deformation process the composite exhibits large plastic deformations. Due to the lack of experiments, we apply an isotropic material behavior for both phases, the metallic matrix and the metallic inclusion. It seems to be reasonable to use an isotropic finite elastoplasticity formulation based on the multiplicative decomposition of the deformation gradient $\mathbf{F} = \mathbf{F}^e \mathbf{F}^p$ in elastic $\mathbf{F}^e$ and plastic $\mathbf{F}^p$ parts, see Kröner (1960), Lee (1969). For details of the thermodynamical formulation as well as for the numerical treatment we refer to Simo (1988, 1992), Simo and Miehe (1992), Peric et al. (1992), Miehe and Stein (1992), and Miehe (1993). In the following we give a brief summary of the used framework. The basic kinematical quantities are

$$\mathbf{b} = \mathbf{F}\,\mathbf{F}^T = \mathbf{F}^e\,\mathbf{b}^p\,(\mathbf{F}^e)^T, \quad \mathbf{b}^p = \mathbf{F}^p\,(\mathbf{F}^p)^T, \text{ and } \quad \mathbf{b}^e = \mathbf{F}^e\,(\mathbf{F}^e)^T, \tag{3}$$

with the spectral decomposition of the elastic finger tensor

$$\mathbf{b}^e = \sum_{A=1}^{3} (\lambda_A^e)^2 \mathbf{n}_A \otimes \mathbf{n}_A \quad, \tag{4}$$

where $\mathbf{n}_A$ denotes the eigenvectors and λ_A^e the eigenvalues of $\mathbf{b}^e$. The stored energy function is assumed to be of the form $\psi = \psi^e(\mathbf{b}^e) + \psi^p(\alpha)$, wherein α denotes the equivalent plastic strains. Following Simo (1992) we use a quadratic free energy function

$$\psi^e = \frac{\lambda}{2}[\epsilon_1^e + \epsilon_2^e + \epsilon_3^e]^2 + \mu[(\epsilon_1^e)^2 + (\epsilon_2^e)^2 + (\epsilon_3^e)^2] \tag{5}$$

in terms of the logarithmic elastic strains $\epsilon_A^e = \log(\lambda_A^e)$; λ and μ are the Lamé constants. In order to model an exponential-type hardening of the individual phases we apply the well-known function

$$\psi^p = y_\infty \alpha - \frac{1}{\eta}(y_0 - y_\infty)\exp(-\eta\alpha) + \frac{1}{2}\,h\,\alpha^2. \tag{6}$$

However, the conjugated stress-like variable, defined as $\beta := \partial_\alpha \psi^p$, is

$$\beta = y_\infty + (y_0 - y_\infty)\exp(-\eta\alpha) + h\,\alpha\,. \tag{7}$$

Herein, y_0 is the initial yield strength, y_∞ and η describe an exponential hardening behavior and h is the slope of a superimposed linear hardening. The yield criterium is given by

$$\phi = ||\mathrm{dev}\boldsymbol{\tau}|| - \sqrt{\frac{2}{3}}\beta \le 0 \quad \text{with} \quad \boldsymbol{\tau} = \sum_{A=1}^{3} \tau_A\,\mathbf{n}_A \otimes \mathbf{n}_A \quad \text{and} \quad \tau_A = \frac{\partial\psi_e}{\partial\epsilon_e}\,. \tag{8}$$

Herein, the Kirchhoff stresses are denoted by $\boldsymbol{\tau}$. The flow rule for the plastic quantity is integrated using an implicit exponential update algorithm, which preserves plastic incompressibility (Weber and Anand (1990), Simo (1992), and Miehe and Stein (1992)). The first Piola-Kirchhoff stresses on the microscale are computed by $\mathbf{P} = \boldsymbol{\tau}\,\mathbf{F}^{-T}$. For the numerical implementation we follow the algorithmic formulation in a material setting as proposed in Klinkel (2000).

2.3 Numerical homogenization

With respect to direct micro-macro approaches relations for the transition between the micro- and macroscale are required. For the definition of the macroscopic quantities we consider a representative volume element (RVE), parametrized in $\mathbf{X} \in \mathcal{B}$, where the microscopic field quantities are determined. In general the macroscopic deformation gradient $\overline{\mathbf{F}}$ and the macroscopic first Piola-Kirchhoff stresses $\overline{\mathbf{P}}$ are defined by suitable surface integrals and volumetric averages

$$\overline{\mathbf{F}} = \frac{1}{vol(\mathrm{RVE})}\int_{\partial\mathcal{B}} \mathbf{x} \otimes \mathbf{N}\,dA \quad \text{and} \quad \overline{\mathbf{P}} = \frac{1}{vol(\mathrm{RVE})}\int_{\partial\mathcal{B}} \mathbf{t_0} \otimes \mathbf{X}\,dA = \frac{1}{vol(\mathrm{RVE})}\int_{\mathcal{B}} \mathbf{P}\,dV\,, \tag{9}$$

wherein $\mathbf{t}_0$ are traction vectors acting on the boundary in the reference configuration. In a variety of applications we are interested in the incremental overall response of the material $\Delta\overline{\mathbf{P}} = \overline{\mathbb{A}} : \Delta\overline{\mathbf{F}}$, wherein $\overline{\mathbb{A}} := \partial_{\overline{F}}\overline{\mathbf{P}}$ denotes the macroscopic nominal moduli. Having such transition relations in hand one is able to compute the micro- and macroscopic boundary value problem. Whereas the macroscopic boundary value problem is standard, the boundary value problem at the microscale is given by

$$\mathrm{Div}[\mathbf{P}] = \mathbf{0} \quad \text{in} \quad \mathcal{B}\,, \tag{10}$$

where we have neglected acceleration terms and volumetric forces. The boundary conditions of the boundary value problem at the microscale are derived from the macro-homogeneity condition, also referred to as Hill–condition, see Hill (1963). It postulates that the macroscopic power is equal to the volumetric average of the microscopic powers, i.e.

$$\overline{\mathbf{P}} \cdot \dot{\overline{\mathbf{F}}} = \frac{1}{vol(\mathrm{RVE})}\int_{\mathcal{B}} \mathbf{P} \cdot \dot{\mathbf{F}}\,dV \quad \Leftrightarrow \quad \frac{1}{vol(\mathrm{RVE})}\int_{\mathcal{B}}(\mathbf{t} - \overline{\mathbf{P}}\mathbf{N}) \cdot (\dot{\mathbf{x}} - \dot{\overline{\mathbf{F}}}\mathbf{X})\,dV = 0\,. \tag{11}$$

Possible boundary conditions are (i) the stress boundary condition, (ii) the linear boundary displacements, and (iii) periodic boundary conditions:

$$\text{(i)}\ \mathbf{t} = \overline{\mathbf{P}}\mathbf{N} \text{ on } \partial\mathcal{B}\,, \quad \text{(ii)}\ \mathbf{x} = \overline{\mathbf{F}}\mathbf{X} \text{ on } \partial\mathcal{B}\,, \quad \text{(iii)}\quad \mathbf{x} = \overline{\mathbf{F}}\mathbf{X} + \tilde{\mathbf{w}},\ \tilde{\mathbf{w}}^+ = \tilde{\mathbf{w}}^-,\ \mathbf{t}^+ = -\mathbf{t}^- \text{ on } \partial\mathcal{B}\,. \tag{12}$$

Note that $\tilde{\mathbf{w}}$ denotes fluctuations of the displacement field and that $(\bullet)^+$, $(\bullet)^-$ means quantities at periodically associated points of the RVE-boundary, for further details we refer to Miehe et al. (1999), Schröder (2000). The basic idea of the FE^2-method is that a microscopic boundary value problem is solved at each Gauss point of a macroscopic boundary value problem. Focusing on periodic boundary conditions (iii) the microscopic BVP is solved and then the average of the resulting microscopic stresses $\overline{\mathbf{P}}$ according to $(9)_2$ is transferred to the macroscale. At the microscale we consider the weak form and its linear increment for a typical finite element

$$G^e(\delta\mathbf{F}, \mathbf{F}) = \int_{\mathcal{B}^e} \delta\tilde{\mathbf{F}} \cdot \mathbf{P}\,dV \quad \text{and} \quad \Delta G^e(\delta\mathbf{F}, \mathbf{F}, \Delta\mathbf{F}) = \int_{\mathcal{B}^e} \delta\tilde{\mathbf{F}} \cdot (\mathbb{A} : \Delta\tilde{\mathbf{F}})\,dV\,, \tag{13}$$

with the microscopic nominal moduli $\mathbb{A} := \partial_F \mathbf{P}$. The fluctuation parts of the actual, virtual and incremental deformation gradient can be approximated by using standard ansatz functions for the fluctuation displacements interpolating between the fluctuation parts of displacements $\tilde{\mathbf{d}}$, virtual displacements $\delta\tilde{\mathbf{d}}$, and incremental displacements $\Delta\tilde{\mathbf{d}}$. Then we obtain the discrete representation of the linearized problem

$$\delta\tilde{\mathbf{D}}^T\{\mathbf{K}\Delta\tilde{\mathbf{D}} + \mathbf{R}\} = 0\,, \tag{14}$$

with the global vectors of incremental fluctuation displacements $\tilde{\mathbf{D}}$ and residual forces $\mathbf{R}$, and with the global microscopic stiffness matrix $\mathbf{K}$. In each iteration the actual increments of displacement fluctuations are computed from (14) and updated, i.e. $\tilde{\mathbf{D}} \Leftarrow \tilde{\mathbf{D}} + \Delta\tilde{\mathbf{D}}$, until $|\mathbf{R}| < tol$, where tol represents the algorithmic tolerance. At the macroscale a standard FE-discretization is considered where the macroscopic moduli which enter the macroscopic stiffness matrix, are computed by

$$\overline{\mathbb{A}} = \langle\mathbb{A}\rangle - \frac{1}{vol(\text{RVE})}\mathbf{L}^T\mathbf{K}^{-1}\mathbf{L} \quad \text{with} \quad \langle\mathbb{A}\rangle = \frac{1}{vol(\text{RVE})}\int_{\mathcal{B}}\mathbb{A}\,dV\,, \tag{15}$$

denoting the classical Voigt bound. Herein, the second additive term represents a softening modulus necessary for the consistent linearization. For its calculation the matrix

$$\mathbf{L} = \mathop{\mathbf{A}}_{e=1}^{nele}\int_{\mathcal{B}^e}\mathbf{B}^T\mathbb{A}\,dV \tag{16}$$

makes use of the same assembling operator applied for assembling the global microscopic stiffness matrix; $\mathbf{B}$ denotes the standard B-matrix. For details on deriving the consistent macroscopic moduli please see e.g. Miehe et al. (1999); Schröder (2000).

3 Method for the construction of SSRVEs

The method for the generation of statistically similar representative volume elements (SSRVEs) is substantiated on the approach for the construction of periodic structures proposed in Povirk (1995). There, the position of circular inclusions with constant and equal diameters is optimized by the minimization of a least-square functional taking into account the side condition that the spectral density of the periodic RVE should be as similar as possible to the one of the non-periodic microstructure. For our further studies we consider the generalized minimization problem

$$\mathcal{L}(\boldsymbol{\gamma}) \to \min \quad \text{with} \quad \mathcal{L}(\boldsymbol{\gamma}) = \sum_{L=1}^{nsm}\omega^{(L)}\mathcal{L}_{SM}^{(L)}(\boldsymbol{\gamma})\,, \tag{17}$$

which has been introduced in Balzani et al. (2009a), see also Balzani et al. (2009b). $\mathcal{L}_{SM}^{(L)}$ describes the least-square functional defined by a suitable difference of a particular statistical measure computed for the real microstructure and for the SSRVE. The number of considered statistical measures is represented by nsm, whereas the weighting factor $\omega^{(L)}$ levels the influence of the individual measures with number (L). For the description of a general inclusion phase morphology in the SSRVE we assume a suitable two-dimensional parameterization controlled by the vector $\boldsymbol{\gamma}$. In our analysis we focus on splines for the parameterization, thus, the coordinates of the sampling points enter $\boldsymbol{\gamma}$.

For an illustration of the main characteristics of the minimization problem a simple test example is given in Balzani et al. (2009a), where the spectral density is taken into account as the main statistical measure. There an assumed real two-dimensional microstructure with one inclusion is considered as a target structure, which is generated by randomly distributing four sampling points. Then a SSRVE is constructed by one spline with four sampling points as well, where three sampling points are set to the values used for the generation of the target structure. Hence, we end up in a problem where only one sampling point is free to move in the optimization process and one is able to visually analyze the objective function plotted over the degrees of freedom. As shown in Balzani et al. (2009a) the resulting objective function is far away from being smooth. Apparently, the computation of the discrete spectral density and the volume fraction takes into account a specific discrete image resolution. Hence, this leads to a non-smooth function and precludes the application of standard gradient-based optimization procedures. This is a rather structural problem since most statistical measures are based on a discrete image characterized by a given resolution. In addition to this, the problem is non-convex and thus, we have to deal with many local minima when increasing the number of degrees of freedom.

To overcome the difficulties arising from the particular minimization problem a moving frame algorithm is applied.

For this purpose random initial sampling point coordinates $x_{0,k}, y_{0,k}$ are generated first, which direct to the sampling point $M_{0,k}$. Then further n_{mov} random points $M_{j,k}(x_{j,k}, y_{j,k})$, $j = 1..n_{mov}$ in a frame of the size $2a \times 2a$ are generated, see Fig. 1a, and the objective function is evaluated for each generated sampling point.
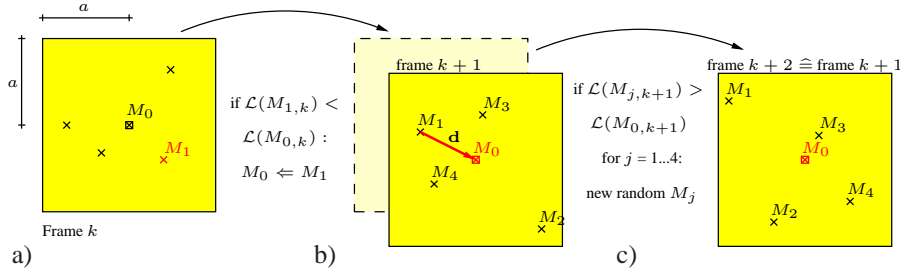

Figure 1: Schematic illustration of moving frame algorithm.

Then the initial sampling point moves to the sampling point $M_{0,k+1}$ defined by the lowest value of $\mathcal{L}$ and the iteration counter is initialized $l_{iter} = 0$, see Fig. 1b . If the frame center remains unaltered, i.e. no lower value of $\mathcal{L}$ is found in this iteration step ($M_{0,k+1} = M_{0,k+2}$), we set $l_{iter} = l_{iter} + 1$, see Fig. 1c. If $l_{iter} = l_{itermax}$ the stopping criterion is reached and the actual minimal value of $\mathcal{L}$ is interpreted as local minimum associated to the starting value. In addition, this procedure is repeated a predefined number of cycles with different random starting values. If a high fraction of minimizers of the individual optimization cycles leads to similar sampling point coordinates, then we choose this result as an appropriate solution. In order to improve the method the frame size a can be modified depending on the difference $|\mathbf{d}|$ and l_{iter}. Furthermore, a combination with a line-search algorithm is implemented, where $\mathcal{L}$ is also evaluated at a number of n_{line} points interconnecting the frame center point M_0 with the random points $M_1, M_2, \dots M_{n_{mov}}$.

The moving-frame algorithm used here is rather a statistical method for finding the minima. Further possiblities for the solution of non-smooth optimization problems can be found in e.g. Kolda et al. (2003), Conn et al. (2009) and Mäkelä and Neittaanmäki (1992). A possible improvement of the minimization algorithm may be obtained by filtering out structural oscillations associated to the non-smoothness in order to obtain at least locally smooth objective function approximations. In this case bundle methods where generalized gradient information is exploited (e.g. Schramm and Zowe (1992)) could be used or the Nelder-Mead method (Nelder and Mead (1965)), if only function evaluations are desireable.

4 Numerical sensitivity analysis of different statistical measures

In this section we study the significance of different statistical measures for the description of the inclusion morphology with respect to the mechanical behavior. Therefore, we compare the mechanical response of a randomly generated microstructure, dealing as a target structure, with the response of different types of SSRVEs. The target structure is obtained by applying the Boolean method, where ellipsoids built from the matrix material are inserted at random points in a pure inclusion material until a predefined volume fraction is reached. For this contribution we consider the target structure shown in Fig. 2a, which is the result of applying the Boolean method for an aspect ratio of the semi-principal axis of $r_x/r_y = 14.3$ and randomly generated $r_x \in [3, 6]$.

$r_x/r_y = 14.3, r_x \in [3, 6]$ $\mathcal{P}_V = 0.1872$ $n_{\mathrm{ele}} = 5452, n_{\mathrm{dof}} = 21930$
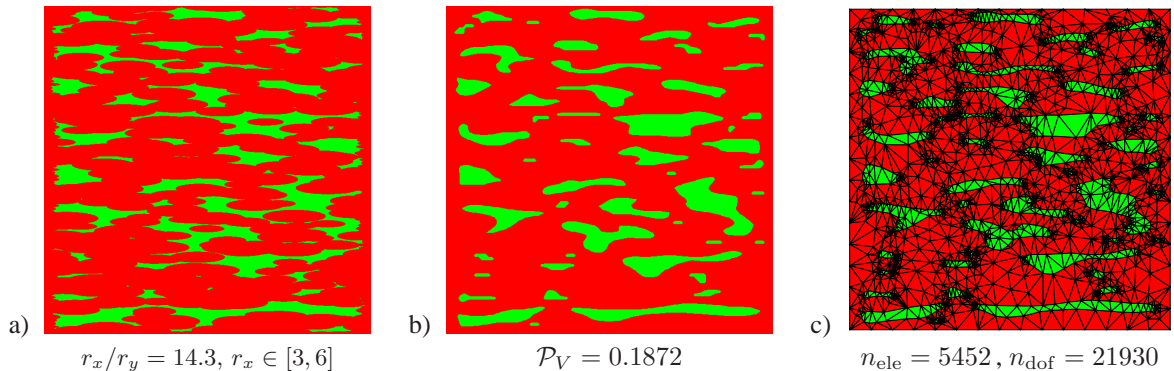
Figure 2: Steps for the generation of the target structure: a) result of the Boolean method, b) smoothed target structure, and c) discretization of the target structure.

The stopping criterion for the Boolean method is given by a volume fraction of the inclusion phase of $0.2 \pm 1\%$. In the next step we smoothen the boundaries of the inclusions in order to avoid singularities, see Fig. 2b, then the resulting volume fraction is $\mathcal{P}_V = 0.1872$. For Finite-Element simulations the smoothened target structure is discretized by 5452 triangular elements with quadratic shape functions, see Fig. 2c. For our analysis we consider three different types of virtual macroscopic experiments: i) horizontal uniaxial tension, ii) vertical uniaxial tension and iii) simple shear, cf. Fig. 3.
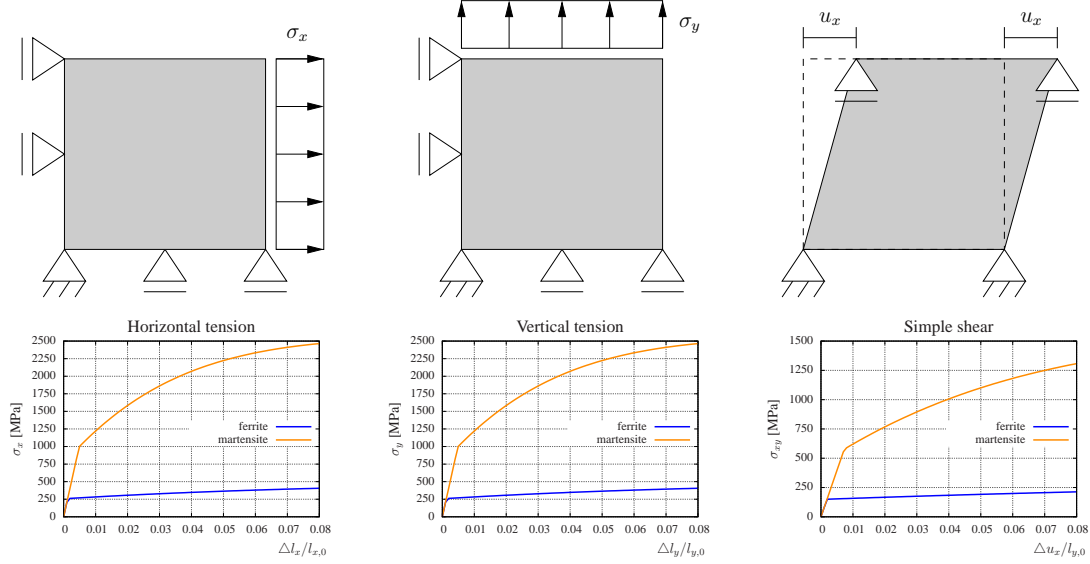

Figure 3: Virtual macroscopic experiments of the pure matrix (ferrite) and inclusion material (martensite); at the microscale periodic boundary conditions are used.

At the microscale the periodic boundary conditions (iii) are used, cf. (12). For the ferritic matrix material and the martensitic inclusions the material parameters given in Table 1 are used. Then a stress-strain response as shown in Fig. 3 is observed for the individual phases in the three virtual experiments.

phase	λ [MPa]	μ [MPa]	y_0 [MPa]	y_∞ [MPa]	η [-]	h [-]
ferrite	118,846.2	79,230.77	260.0	580.0	9.0	70.0
martensite	118,846.2	79,230.77	1000.0	2750.0	35.0	10.0

Table 1: Material parameters of the single phases

The SSRVEs are constructed considering several combinations of statistical measures as optimization criteria. Since the volume fraction is an important overall information with view to the influence of the morphology on the mechanical properties we take it into account for all SSRVE constructions given in this contribution. Then, the associated least-square functional reads

$$\mathcal{L}^{(1)} := \mathcal{L}_V(\gamma) = \left(1 - \frac{\mathcal{P}_V^{SSRVE}(\gamma)}{\mathcal{P}_V^{real}} \right)^2 , \tag{18}$$

which is used within the general minimization problem (17). Since we analyze two-dimensional images the volume fractions $\mathcal{P}_V^{real}$ and $\mathcal{P}_V^{SSRVE}$ required for the computation of $\mathcal{L}_V$ are computed by

$$\mathcal{P}_V := \frac{V_I}{V} , \tag{19}$$

where V_I denotes the area of the inclusion phase and V the total area of the considered microstructure image. The computation of the volume fraction is performed directly from the binary images of the given target structure and the SSRVE.

4.1 Sensitivity for two different statistical measures

In a first step we study the significance of several statistical measures for the generation of SSRVEs with respect to their mechanical behavior compared with the target structure. As already mentioned the volume fraction is in all cases an additional constraint in the optimization process.

4.1.1 Specific internal surface

In Ohser and Mücklich (2000) the specific internal surface is mentioned as one basic parameter to describe microstructure morphology. It seems to be a suitable measure for the specification of the inclusion phase's distribution. In the general three-dimensional case this parameter is given by

$$\mathcal{P}_S^{3D} := \frac{S_I}{V}\,, \tag{20}$$

with the interface area S_I separating the inclusion from the matrix material and the total volume V of the considered microstructure. Here we focus on the two-dimensional case and so this parameter can be calculated by

$$\mathcal{P}_S := \frac{4}{\pi} L_A\,, \tag{21}$$

wherein L_A is the specific boundary line length between the two phases. It is mentioned that Eq. (21) can be derived from Crofton's slice formulas for compact bodies, see Ohser and Mücklich (2000). Then the associated least-square functional reads

$$\mathcal{L}^{(2)} := \mathcal{L}_S(\gamma) = \left(1 - \frac{\mathcal{P}_S^{SSRVE}(\gamma)}{\mathcal{P}_S^{real}} \right)^2\,, \tag{22}$$

and together with the volume fraction functional (18) we get the first minimization problem

$$\mathcal{L}_1(\gamma) = \sum_{L=1}^{2} \omega^{(L)} \mathcal{L}^{(L)} = \omega_V \mathcal{L}_V(\gamma) + \omega_S \mathcal{L}_S(\gamma) \rightarrow \min \quad \text{with} \quad \omega_V = \omega_S = 1\,, \tag{23}$$

For the parameterization of the inclusion morphology of the SSRVE splines are used, thus, the coordinates of the sampling points arranged in γ represent the degree of freedom in the optimization problem. Here we take into account four types of inclusion parameterization: one inclusion with three sampling points (type I) leading to convex inclusions, one inclusion with four sampling points (type II), and two inclusions with three and four sampling points each (type III and type IV), respectively. The results of the optimization process considering the microstructure in Fig. 2 as target are shown in Fig. 4. The decreasing values of the objective function together with an increasing number of sampling points can be observed. This is an expected behavior as we know that the number of sampling points reflects the degree of freedom for the generation, thus also the complexity of the inclusions. But the higher complexity implicates a larger quantity of finite elements in the discretization. This is a non-negligible aspect in the context of replacing a RVE with an arbitrary complex inclusion morphology by a simpler one with similar mechanical behavior.

Type I: $n_{\text{dof}} = 2394$	Type II: $n_{\text{dof}} = 2762$	Type III: $n_{\text{dof}} = 4058$	Type IV: $n_{\text{dof}} = 4650$

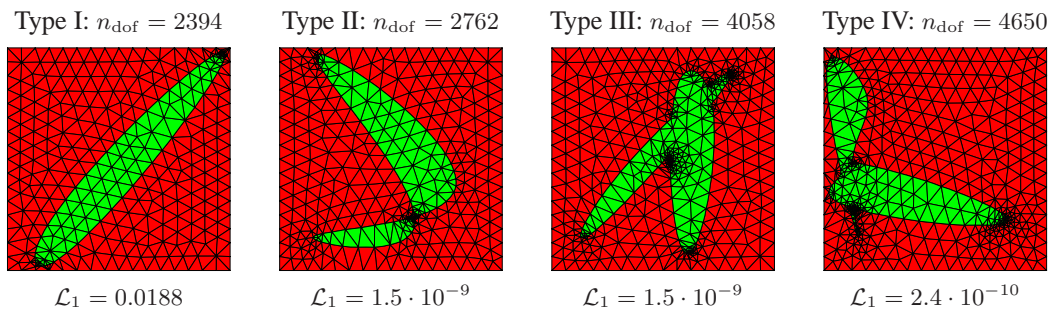| $\mathcal{L}_1 = 0.0188$	$\mathcal{L}_1 = 1.5 \cdot 10^{-9}$	$\mathcal{L}_1 = 1.5 \cdot 10^{-9}$	$\mathcal{L}_1 = 2.4 \cdot 10^{-10}$

Figure 4: Discretization of the SSRVEs resulting from the minimization of $\mathcal{L}_1$.

In order to study the SSRVEs capability to reflect the mechanical response of the target structure we compare the stress-strain response of the SSRVEs with the response of the target structure in the three virtual experiments, see Fig 3. The resulting stress-strain curves are shown in Fig. 5. For the estimation of the accuracy we compute the relative errors

$$r_x^{(i)} = \frac{\sigma_{x,i}^{real} - \sigma_{x,i}^{SSRVE}}{\sigma_{x,i}^{real}} , \quad r_y^{(i)} = \frac{\sigma_{y,i}^{real} - \sigma_{y,i}^{SSRVE}}{\sigma_{y,i}^{real}} , \quad r_{xy}^{(i)} = \frac{\sigma_{xy,i}^{real} - \sigma_{xy,i}^{SSRVE}}{\sigma_{xy,i}^{real}} , \tag{24}$$

as the deviation of the SSRVE stress response from the target structure response at each evaluation point i. To consider relative quantities is important here in order to be able to compare the different virtual experiments. Then the average error for each virtual experiment is computed by

$$\widetilde{r} = \sqrt{\frac{1}{n} \sum_{i=1}^{n} \left[r^{(i)} \left(\frac{i}{n} \triangle l_{\max}/l_0 \right) \right]} . \tag{25}$$

As a comparative measure we define the overall average error

$$\widetilde{r}_\varnothing = \frac{1}{3} \left(\widetilde{r}_x + \widetilde{r}_y + \widetilde{r}_{xy} \right) . \tag{26}$$

The error values for the experiments based on the SSRVEs generated through $\mathcal{L}_1$ are shown in Table 2.
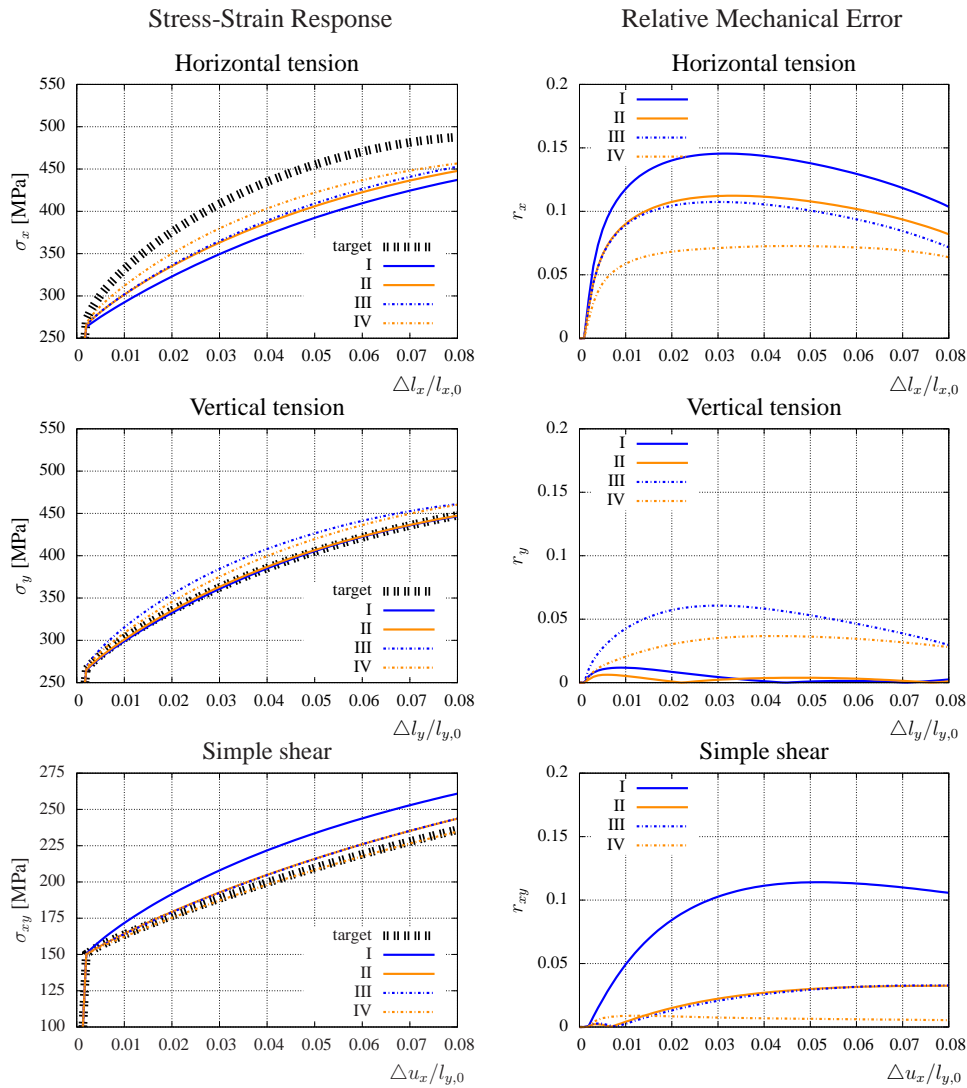

Figure 5: Results of the virtual experiments using the discretizations of the SSRVEs based on $\mathcal{L}_1$ (Figure 4).

In Fig. 5 the stress-strain curves of each SSRVEs shows different accuracies with respect to the virtual experiments. In the first test, the horizontal tension, the mechanical errors decrease depending on the complexity of the SSRVE, but also type IV has an error above five percent at most evaluation points. On the other hand in the vertical tension the behavior differs totally. Here the types I and II show a good agreement with the results of the target structure ($r_y < 1\%$) and the both other types differ more. But all errors are lower compared to them from the horizontal tension. The simple shear experiments show qualitatively similar results as we have seen in the horizontal tension test. But the error values particularly the higher order types are at a lower level, see also Table 2. If we take a look at the overall average error in Table 2 we see that the specific internal surface and sufficient complexity of the SSRVEs inclusions yield slightly the mechanical response of the target structure. But the significant different accuracies comparing the both tension experiments show that the specific internal surface does not contain enough directional information of the inclusion morphology and is therefore not able to cover macroscopic anisotropy information. Thus, we have to take another statistical measure into account to describe this characteristic of a microstructure.

SSRVE type	$\mathcal{L}_1$ [-]	$\mathcal{L}_V$ [-]	$\mathcal{L}_S$ [-]	n_{ele} [-]	$\widetilde{r}_x$ [%]	$\widetilde{r}_y$ [%]	$\widetilde{r}_{xy}$ [%]	$\widetilde{r}_{\varnothing}$ [%]
I	0.0188	0.0	0.0188	566	12.44 ± 2.83	0.39 ± 0.40	9.18 ± 3.18	7.34
II	$1.5 \cdot 10^{-9}$	0.0	$1.5 \cdot 10^{-9}$	658	9.67 ± 2.18	0.27 ± 0.16	2.23 ± 1.09	4.06
III	$1.5 \cdot 10^{-9}$	0.0	$1.5 \cdot 10^{-9}$	982	9.12 ± 2.09	4.68 ± 1.35	2.16 ± 1.12	5.32
IV	$2.4 \cdot 10^{-10}$	0.0	$2.4 \cdot 10^{-10}$	1130	6.52 ± 1.43	3.00 ± 0.85	0.66 ± 0.17	3.40

Table 2: Values of the objective function $\mathcal{L}_1$ and the errors $\widetilde{r}$ using the SSRVEs shown in Figure 4.

4.1.2 Specific integral of mean curvature

As an other basic parameter for the descrictpion of the morphology of heterogeneous microstructures the specific integral of mean curvature for the general three-dimensional case is defined as

$$\mathcal{P}_M^{3D} := \frac{1}{2V} \int_S \left(\min_\beta[\kappa] + \max_\beta[\kappa] \right) ds \,, \tag{27}$$

cf. Ohser and Mücklich (2000). The integral is evaluated over the interface S between the inclusion and matrix phase of the average curvature $\kappa := \kappa(\beta)$ varying with direction β in the tangential plane. For the two-dimensional case the specific integral of mean curvature can be calculated by

$$\mathcal{P}_M := 2\pi X_A \,, \tag{28}$$

with the specific Euler number following Ohser and Mücklich (2000). For the optimization process we formulate the associated least-square functional

$$\mathcal{L}^{(2)} := \mathcal{L}_M(\gamma) = \left(1 - \frac{\mathcal{P}_M^{SSRVE}(\gamma)}{\mathcal{P}_M^{real}} \right)^2 \,, \tag{29}$$

Type I: $n_{\text{dof}} = 2370$ Type II: $n_{\text{dof}} = 2642$ Type III: $n_{\text{dof}} = 3178$ Type IV: $n_{\text{dof}} = 6522$

$\mathcal{L}_2 = 0.2648$ $\mathcal{L}_2 = 8.5 \cdot 10^{-4}$ $\mathcal{L}_2 = 8.5 \cdot 10^{-4}$ $\mathcal{L}_2 = 8.5 \cdot 10^{-4}$
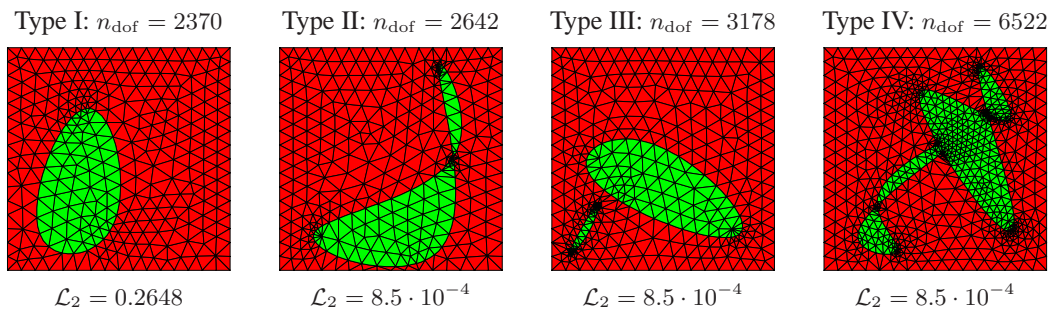
Figure 6: Discretization of the SSRVEs resulting from the minimization of $\mathcal{L}_2$.

As before we also consider the functional (18) and get the second minimization problem

$$\mathcal{L}_2(\boldsymbol{\gamma}) = \sum_{L=1}^{2} \omega^{(L)} \mathcal{L}^{(L)} = \omega_V \mathcal{L}_V(\boldsymbol{\gamma}) + \omega_M \mathcal{L}_M(\boldsymbol{\gamma}) \rightarrow \min \quad \text{with} \quad \omega_V = \omega_M = 1 \,. \tag{30}$$

The vector $\boldsymbol{\gamma}$ contains the sampling points for the generation of SSRVEs by splines. We again consider four different types of inclusion parametrization, for details see Section 4.1.1. As the result from the optimization we get the four SSRVEs shown in Fig. 6.
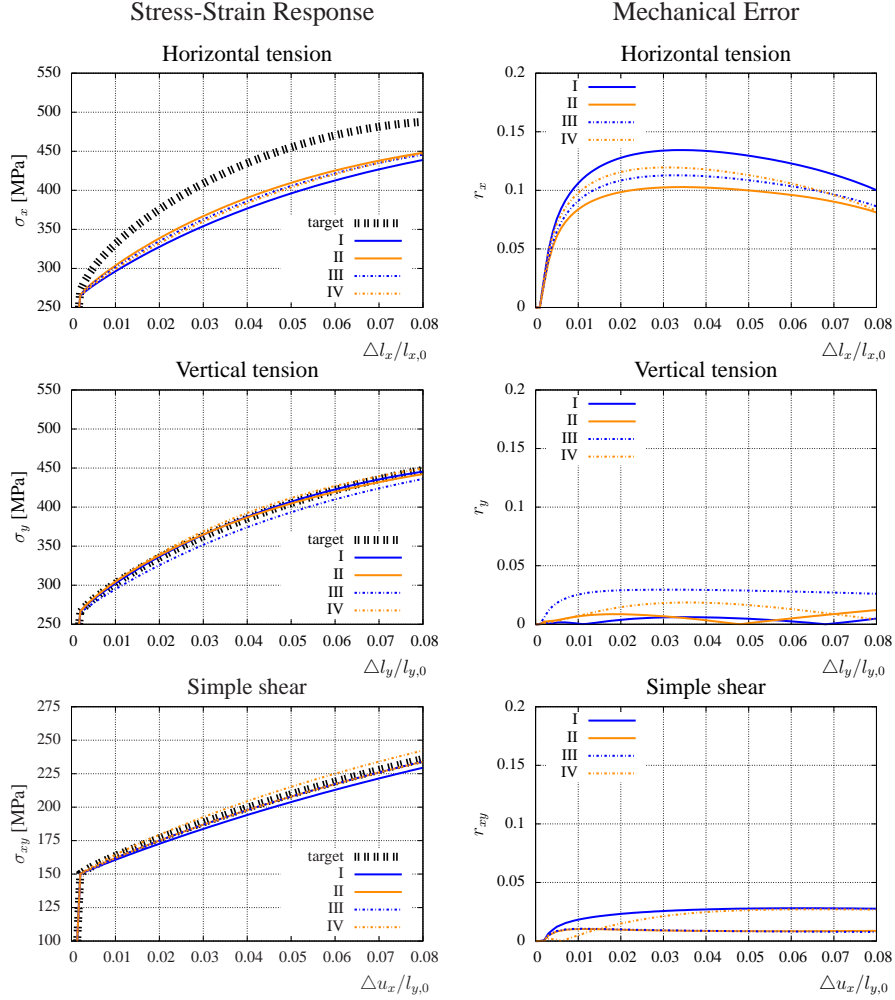

Figure 7: Results of the virtual experiments using the discretizations based on $\mathcal{L}_2$ (Figure 6).

The stress-strain curves of the three virtual experiments (Fig. 3) performed with the discretized SSRVEs from Fig. 6 are shown in Fig. 7 compared to the results of the target strcuture. For the comparision of these results we compute again the errors (24)-(26), which are listed in Table 3.

SSRVE type	$\mathcal{L}_2$ [-]	$\mathcal{L}_V$ [-]	$\mathcal{L}_M$ [-]	n_{ele} [-]	$\widetilde{r}_x$ [%]	$\widetilde{r}_y$ [%]	$\widetilde{r}_{xy}$ [%]	$\widetilde{r}_{\varnothing}$ [%]
I	0.2648	0.0	0.2648	560	11.58 ± 2.66	0.33 ± 0.20	2.40 ± 0.65	4.77
II	$8.5 \cdot 10^{-4}$	0.0	$8.5 \cdot 10^{-4}$	628	9.02 ± 2.00	0.58 ± 0.31	0.85 ± 0.18	3.48
III	$8.5 \cdot 10^{-4}$	0.0	$8.5 \cdot 10^{-4}$	762	9.79 ± 2.21	2.65 ± 0.57	0.84 ± 0.19	4.43
IV	$8.5 \cdot 10^{-4}$	0.0	$8.5 \cdot 10^{-4}$	1598	10.20 ± 2.32	1.22 ± 0.54	1.99 ± 0.90	4.47

Table 3: Values of the objective function $\mathcal{L}_2$ and the errors $\widetilde{r}$ using the SSRVEs shown in Figure 6.

In Fig. 7 the stress-strain curves for the vertical tension and the simple shear tests of the SSRVEs show good agreements with the results of the target structure. In both cases the error is lower than 5% in all evaluation points. But in the first test, the horizontal tension, all types of SSRVE have errors above 10% in several evaluation points.

The errors in Table 3 confirm the observation from the stress-strain curves and also shows that an increasing number of sampling points does not achieve better results. The errors of the horizontal and the vertical tests differ again in a strong manner and so the specific integral of mean curvature is again not a parameter covering directional information of the microstructure. Also a larger range in the values of the overall average errors can be observed in Table 2, which are associated to the volume fraction and the specific internal surface, compared to the results in this section here.

4.1.3 Spectral density

The results from Section 4.1.1 and 4.1.2 show that we need to consider statistical measures which cover directional information. A possibility is the (discrete) spectral density (SD) for the inclusion phase of a binary image, which is computed by the multiplication of the (discrete) Fourier transform with its conjugate complex. The discrete SD is defined by

$$\mathcal{P}_{SD}(m,k) := \frac{1}{2\pi\,N_x\,N_y}\,|\mathcal{F}(m,k)|^2 \tag{31}$$

with the Fourirer transform given by

$$\mathcal{F}^I(m,k) = \sum_{p=1}^{N_x}\sum_{q=1}^{N_y} \exp\left(\frac{2\,i\,\pi\,m\,p}{N_x}\right)\exp\left(\frac{2\,i\,\pi\,k\,q}{N_y}\right)\chi^I(p,q)\,. \tag{32}$$

The maximal numbers of pixels in the considered binary image are given by N_x and N_y; the indicator function is defined as

$$\chi := \begin{cases} 1, & \text{if } (p,q) \text{ is in inclusion phase} \\ 0, & \text{else}\,. \end{cases} \tag{33}$$

For the consideration of the SD in the optimization problem we write the least-square functional

$$\mathcal{L}^{(2)} := \mathcal{L}_{SD}(\boldsymbol{\gamma}) = \frac{1}{N_x\,N_y}\sum_{m=1}^{N_x}\sum_{k=1}^{N_y}\left(\mathcal{P}_{SD}^{real}(m,k) - \mathcal{P}_{SD}^{SSRVE}(m,k,\boldsymbol{\gamma})\right)^2\,, \tag{34}$$

and together with (18) we get the minimization problem

$$\mathcal{L}_3(\boldsymbol{\gamma}) = \sum_{L=1}^{2}\omega^{(L)}\mathcal{L}^{(L)} = \omega_V\mathcal{L}_V(\boldsymbol{\gamma}) + \omega_{SD}\mathcal{L}_{SD}(\boldsymbol{\gamma}) \;\rightarrow\; \min \quad\text{with}\quad \omega_V = \omega_{SD} = 1\,. \tag{35}$$

The evaluation of the functional (34) requires a more detailed treatment since the others are scalar-valued. In order to get reasonable results and to obtain an efficient optimization procedure it may be necessary not to consider the spectral density at a very fine resolution level (N_x and N_y very large). Therefore, first the SD is computed at a high resolution. Second, the spectral density is rebinned such that a lower resolution is obtained, which means that N_x and N_y are decreased. Finally, the SD is normalized by dividing by its maximum value $\max_{m,k}[\mathcal{P}_{SD}(m,k)]$. In Fig. 8 the resulting SSRVEs from the optimization process are shown, whereas the same types of SSRVE

| Type I: $n_{\mathrm{dof}} = 2314$ | Type II: $n_{\mathrm{dof}} = 3250$ | Type III: $n_{\mathrm{dof}} = 4350$ | Type IV: $n_{\mathrm{dof}} = 5666$ |

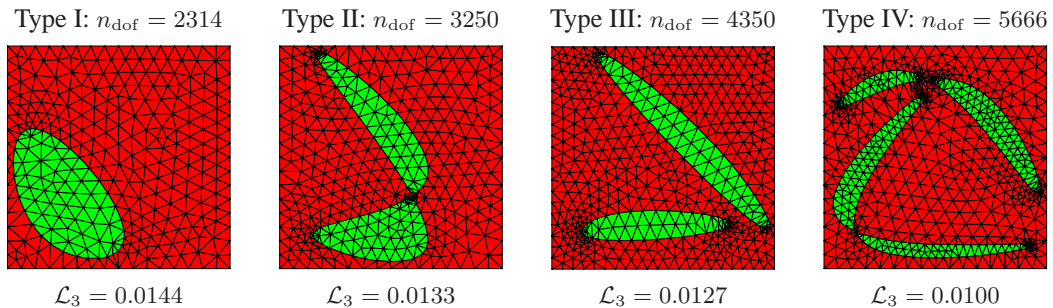| $\mathcal{L}_3 = 0.0144$ | $\mathcal{L}_3 = 0.0133$ | $\mathcal{L}_3 = 0.0127$ | $\mathcal{L}_3 = 0.0100$ |

Figure 8: Discretization of the SSRVEs resulting from the minimization of $\mathcal{L}_3$.
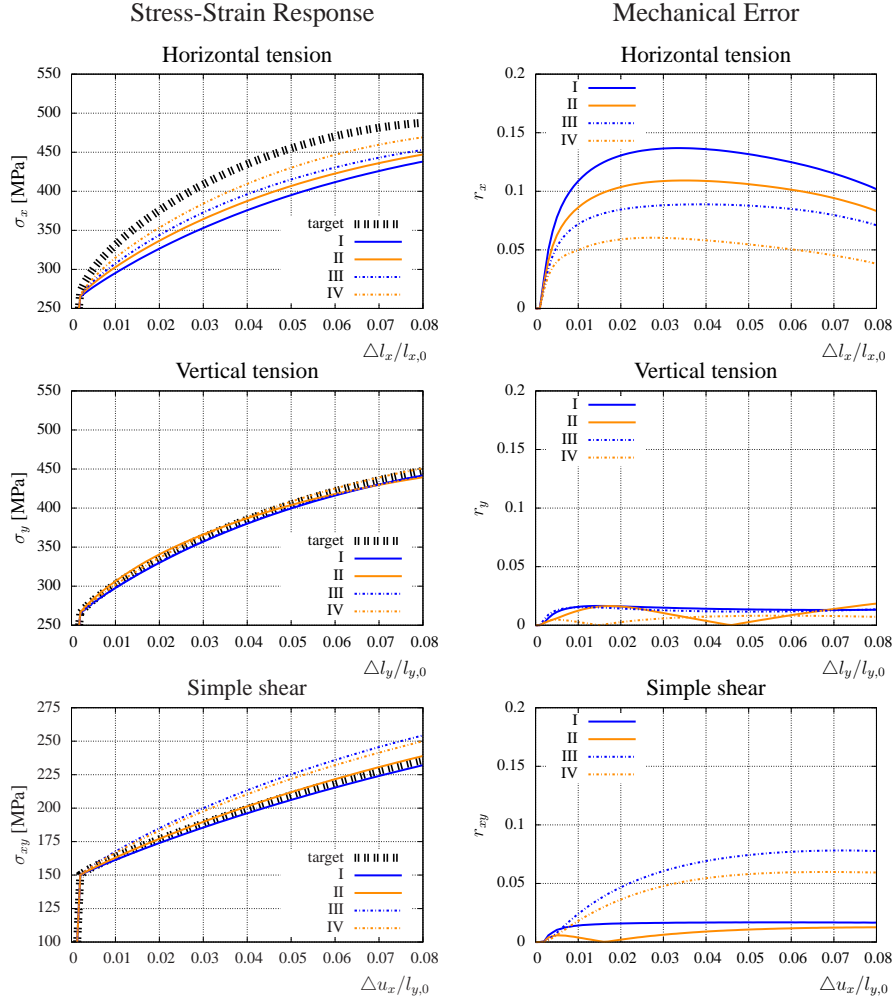
Figure 9: Results of the virtual experiments using the discretizations of the SSRVEs based on $\mathcal{L}_3$ (Figure 8).

parametrization are considered as described in detail in section 4.1.1. Again for the discretized SSRVEs in Fig. 8 we perform the three virtual experiments (Fig. 3) and compute the errors with respect to the results of the target structure by (24)-(26). As a result we get the stress-strain curves in Fig. 9 and the errors in Table 4.

From the stress-strain curves we see the best accuracies for the vertical tension test ($< 2.5\%$). A similar result can be observed from the curve of type I and II in the simple shear test. But there both other types have a higher deviation. The horizontal tension test shows a wide spectrum in the mechanical error, from nearly 14% for type I to 6% for type VI. This experiment shows a decreasing deviation together with an increasing number of sampling points, which could be put on a level with the complexity of the SSRVE. Also the values of the objective function in Table 4 show the same behavior.

It seems that the spectral density is a statistical measure for the description of directional information but the prediction of the objective function does not correspond with the mechanical behavior in details. So our next step is to analyse the combination of more than two statistical measures.

SSRVE type	$\mathcal{L}_3$ [-]	$\mathcal{L}_V$ [-]	$\mathcal{L}_{SD}$ [-]	n_{ele} [-]	$\widetilde{r}_x$ [%]	$\widetilde{r}_y$ [%]	$\widetilde{r}_{xy}$ [%]	$\widetilde{r}_{\varnothing}$ [%]
I	0.0144	0.0	0.0144	546	11.80 ± 2.70	1.35 ± 0.30	1.53 ± 0.35	4.89
II	0.0133	$2.9 \cdot 10^{-7}$	0.0133	780	9.48 ± 2.15	0.96 ± 0.54	0.78 ± 0.41	3.74
III	0.0127	$1.1 \cdot 10^{-6}$	0.0127	1046	7.85 ± 1.74	1.24 ± 0.25	5.83 ± 2.37	4.97
IV	0.0100	$3.5 \cdot 10^{-5}$	0.0100	1384	5.04 ± 1.14	0.59 ± 0.25	4.52 ± 1.84	3.38

Table 4: Values of the objective function $\mathcal{L}_3$ and the errors $\widetilde{r}$ using the SSRVEs shown in Figure 8.

4.2 Combination of three different statistical measures

As in the analysis in section 4.1 we take into account the volume fraction for all optimization processes as a standard parameter. In addition, as an outcome of the latter section, we also consider the spectral density as a suitable statistical measure, because of its possibility to cover directional information of the morphology. We combine these both with first, the specific surface and second, the specific integral of mean curvature.

4.2.1 Specific internal surface

For the consideration of the volume fraction, the spectral density and the specific internal surface during the generation of the SSRVEs we set $\mathcal{L}^{(1)} = \mathcal{L}_V$, $\mathcal{L}^{(2)} = \mathcal{L}_{SD}$, $\mathcal{L}^{(3)} = \mathcal{L}_S$ and formulate the following minimization problem

$$\mathcal{L}_4(\boldsymbol{\gamma}) = \omega_V \mathcal{L}_V(\boldsymbol{\gamma}) + \omega_{SD}\mathcal{L}_{SD}(\boldsymbol{\gamma}) + \omega_S \mathcal{L}_S(\boldsymbol{\gamma}) \ \rightarrow \ \min \quad \text{with} \quad \omega_V = \omega_{SD} = \omega_S = 1 \,, \tag{36}$$

using the objective functions (18), (34) and (22). We also consider the same types of SSRVE parametrization during the optimization process as before and the resulting discretizations are shown in Figure 10.
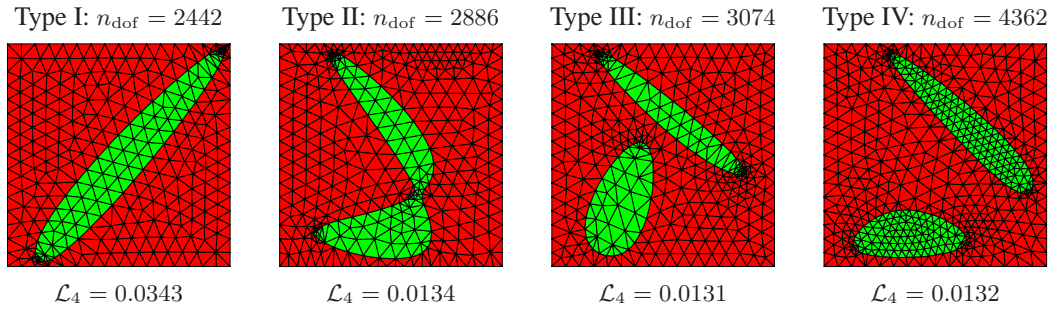
Type I: $n_{\text{dof}} = 2442$ Type II: $n_{\text{dof}} = 2886$ Type III: $n_{\text{dof}} = 3074$ Type IV: $n_{\text{dof}} = 4362$

$\mathcal{L}_4 = 0.0343$ $\qquad$ $\mathcal{L}_4 = 0.0134$ $\qquad$ $\mathcal{L}_4 = 0.0131$ $\qquad$ $\mathcal{L}_4 = 0.0132$

Figure 10: Discretization of the SSRVEs resulting from the minimization of $\mathcal{L}_4$.

For the comparison of the results from the virtual experiments we compute the errors (24)-(26). In Fig. 11 the stress-strain curves of the virtual experiments for the target structure and the SSRVEs are shown and the errors are listed in Table 5.

SSRVE type	$\mathcal{L}_4$ [-]	$\mathcal{L}_V$ [-]	$\mathcal{L}_{SD}$ [-]	$\mathcal{L}_S$ [-]	n_{ele} [-]	$\widetilde{r}_x$ [%]	$\widetilde{r}_y$ [%]	$\widetilde{r}_{xy}$ [%]	$\widetilde{r}_\varnothing$ [%]
I	0.0343	$1.1{\cdot}10^{-6}$	0.0155	0.0188	578	12.44 ± 2.83	0.41 ± 0.39	9.12 ± 3.16	7.32
II	0.0134	$1.1{\cdot}10^{-6}$	0.0134	$1.3{\cdot}10^{-7}$	680	9.07 ± 2.05	3.44 ± 1.15	0.61 ± 0.30	4.37
III	0.0131	$1.1{\cdot}10^{-6}$	0.0131	$5.7{\cdot}10^{-6}$	736	11.20 ± 2.54	1.56 ± 0.33	3.50 ± 1.52	5.42
IV	0.0132	$2.9{\cdot}10^{-7}$	0.0132	$9.9{\cdot}10^{-7}$	1058	10.80 ± 2.44	2.59 ± 0.53	4.43 ± 1.82	5.94

Table 5: Values of the objective function $\mathcal{L}_4$ and the errors $\widetilde{r}$ using the SSRVEs shown in Figure 10.

The stress-strain curves do not show a better result compared to the one based on the SSRVEs from the optimization without the specific internal surface. In fact, the simple shear test shows a worse result than Fig. 8 and it seems that the directional information provided by the spectral density does not influence the mechanical response in any case. The values of the objective function and of the errors in Table 5 do not decrease with increasing degrees of freedom for the SSRVE generation. So the application of the specific internal surface combined with the volume fraction and the spectral density does not improve the accuracy of the mechanical results with respect to the target structure. In some cases the opposite effect can be observed.
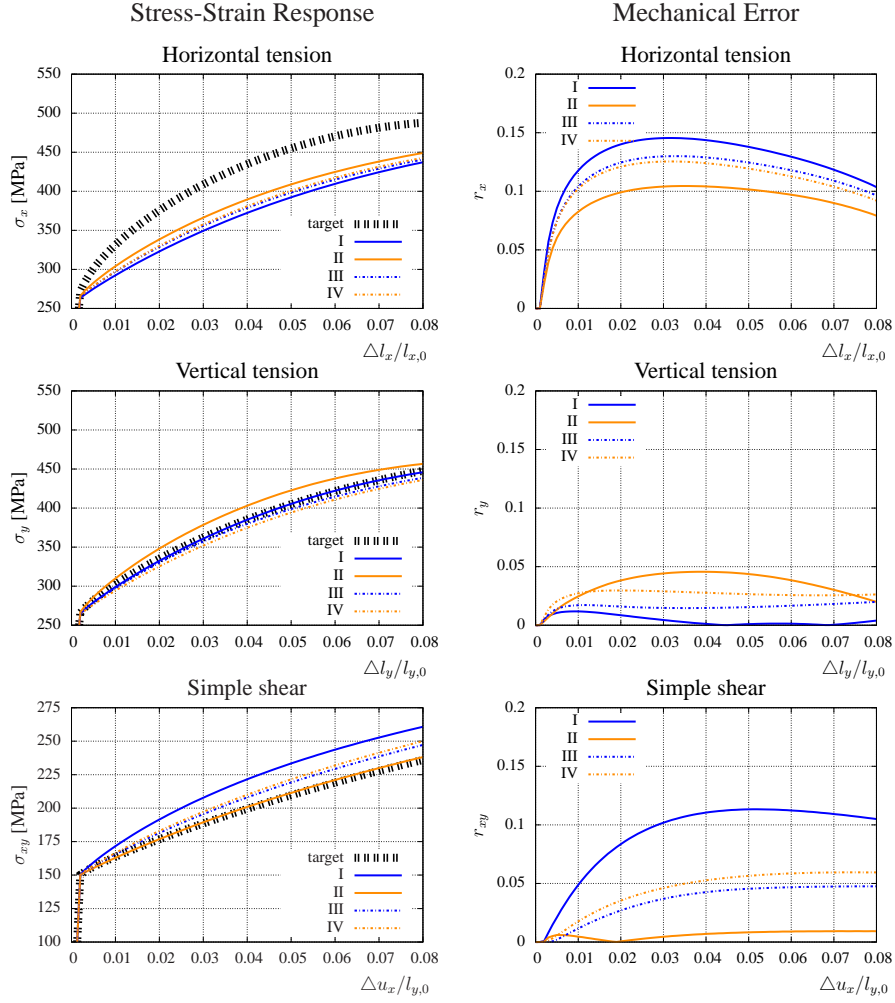
Figure 11: Results of the virtual experiments using the discretizations of the SSRVEs base on $\mathcal{L}_4$ (Figure 10).

4.2.2 Specific integral of mean curvature

Instead of the specific internal surface we now apply the objective function (29) of the specific integral of mean curvature to the minimization problem, set $\mathcal{L}^{(1)} = \mathcal{L}_V$, $\mathcal{L}^{(2)} = \mathcal{L}_{SD}$, $\mathcal{L}^{(3)} = \mathcal{L}_M$ and end up with

$$\mathcal{L}_5(\boldsymbol{\gamma}) = \omega_V \mathcal{L}_V(\boldsymbol{\gamma}) + \omega_{SD} \mathcal{L}_{SD}(\boldsymbol{\gamma}) + \omega_M \mathcal{L}_M(\boldsymbol{\gamma}) \rightarrow \min \quad \text{with} \quad \omega_V = \omega_{SD} = \omega_M = 1 \,. \tag{37}$$

From the optimization process we get the SSRVEs in Fig. 12, where we consider the already mentioned four types of parametrization through a different number of sampling points. There, an increasing number of elements for the discretization of the SSRVEs together with an increasing number of sampling points can be observed.
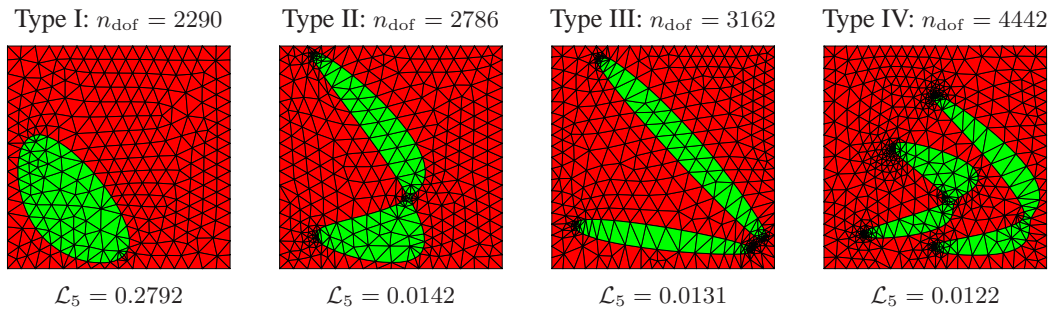

Figure 12: Discretization of the SSRVEs resulting from the minimization of $\mathcal{L}_5$.

The errors listed in Table 6 and computed by (24)-(26) show again, that a higher level of complexity for the SSRVE generation produces a lower deviation. This behavior is also reflected by the values of the objective function.

SSRVE type	$\mathcal{L}_5$ [-]	$\mathcal{L}_V$ [-]	$\mathcal{L}_{SD}$ [-]	$\mathcal{L}_M$ [-]	n_{ele} [-]	$\widetilde{r}_x$ [%]	$\widetilde{r}_y$ [%]	$\widetilde{r}_{xy}$ [%]	$\widetilde{r}_\varnothing$ [%]
I	0.2792	0.0	0.0144	0.2648	540	11.80 ± 2.70	1.49 ± 0.32	1.56 ± 0.36	4.95
II	0.0142	$1.1 \cdot 10^{-6}$	0.0133	$8.5 \cdot 10^{-4}$	664	9.57 ± 2.15	2.84 ± 1.17	0.89 ± 0.48	4.44
III	0.0131	$2.6 \cdot 10^{-6}$	0.0123	$8.5 \cdot 10^{-4}$	750	6.35 ± 1.41	0.21 ± 0.19	6.61 ± 2.67	4.39
IV	0.0122	$2.6 \cdot 10^{-6}$	0.0113	$8.5 \cdot 10^{-4}$	1070	8.51 ± 1.88	0.26 ± 0.13	1.82 ± 0.95	3.53

Table 6: Values of the objective function $\mathcal{L}_5$ and the errors $\widetilde{r}$ using the SSRVEs shown in Figure 12.

But we can not observe a significantly lower deviation than the ones in Table 4 associated to the SSRVEs based only on the volume fraction and the spectral density.
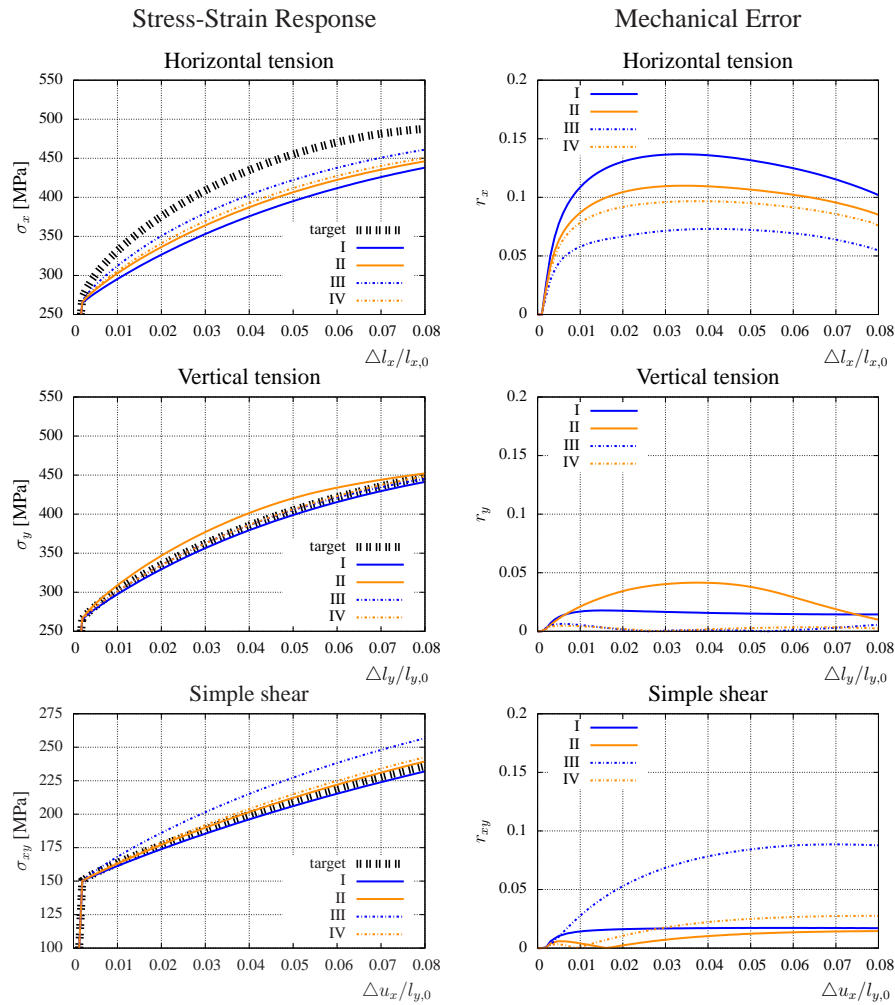

Figure 13: Results of the virtual experiments using the discretizations of the SSRVEs based on $\mathcal{L}_5$ (Figure 12).

The overall average errors of the virtual experiments in this section are in a smaller range as the errors of the results in the previous section, where we consider the volume fraction, spectral density and specific internal surface. This behavior was already recognized in sections 4.1.1 and 4.1.2 by comparing the results of the SSRVEs generated without consideration of the spectral density.

4.3 Combination of all four statistical measures

At least we consider all statistical measures which are discussed in this contribution. Using the objective function (18), (22), (29) and (34) we formulate the minimization problem

$$\mathcal{L}_6(\boldsymbol{\gamma}) = \omega_V \mathcal{L}_V(\boldsymbol{\gamma}) + \omega_A \mathcal{L}_A(\boldsymbol{\gamma}) + \omega_M \mathcal{L}_M(\boldsymbol{\gamma}) + \omega_{SD}\mathcal{L}_{SD}(\boldsymbol{\gamma}) \rightarrow \min \tag{38}$$
$$\text{with} \quad \omega_V = \omega_A = \omega_M = \omega_{SD} = 1\,,$$

for the generation of the four different types of SSRVE. The results of the optimization process are depicted in Fig. 14.

Type I: $n_{\mathrm{dof}} = 2322$ Type II: $n_{\mathrm{dof}} = 3426$ Type III: $n_{\mathrm{dof}} = 3034$ Type IV: $n_{\mathrm{dof}} = 4690$

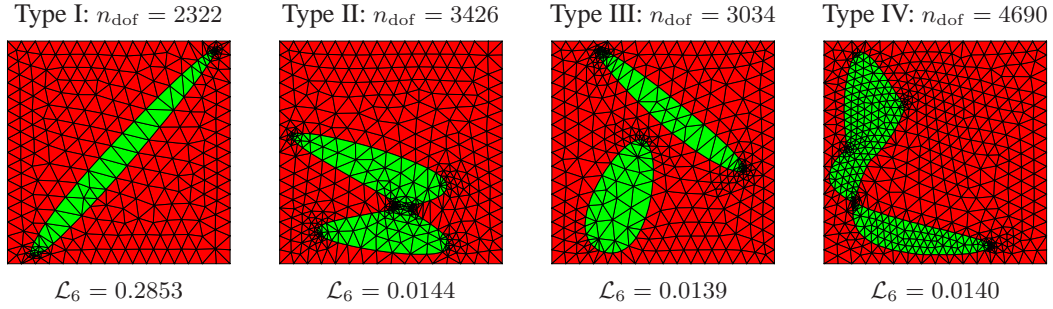$\mathcal{L}_6 = 0.2853$ $\mathcal{L}_6 = 0.0144$ $\mathcal{L}_6 = 0.0139$ $\mathcal{L}_6 = 0.0140$

Figure 14: Discretization of the SSRVEs resulting from the minimization of $\mathcal{L}_6$.

The stress-strain curves in Fig. 15 do not show better accuracies than the results from the previous section, where we do not consider the specific internal surface. On the contrary we can observe larger error values up to nearly 17% in the horizontal tension test. Computing the average errors by (24)-(26) and listing them in Table 7 we see again the worse results. Although the value of the objective function nearly decreases from one complexity level to the next one, the overall average error does not show the same behavior.

SSRVE type	$\mathcal{L}_6$ [-]	$\mathcal{L}_V$ [-]	$\mathcal{L}_{SD}$ [-]	$\mathcal{L}_S$ [-]	$\mathcal{L}_M$ [-]	n_{ele} [-]	$\widetilde{r}_x$ [%]	$\widetilde{r}_y$ [%]	$\widetilde{r}_{xy}$ [%]	$\widetilde{r}_{\varnothing}$ [%]
I	0.2853	0.1653	0.0160	0.0301	0.0739	548	14.43 ± 3.30	2.97 ± 0.61	6.18 ± 2.23	7.86
II	0.0144	$2.9 \cdot 10^{-7}$	0.0136	$2.2 \cdot 10^{-8}$	$8.5 \cdot 10^{-4}$	824	6.92 ± 1.55	0.40 ± 0.20	0.35 ± 0.29	2.56
III	0.0139	$1.1 \cdot 10^{-6}$	0.0131	$5.7 \cdot 10^{-6}$	$8.5 \cdot 10^{-4}$	726	11.20 ± 2.55	1.62 ± 0.37	3.48 ± 1.52	5.43
IV	0.0140	0.0	0.0132	$2.2 \cdot 10^{-8}$	$8.5 \cdot 10^{-4}$	1140	8.80 ± 1.94	1.69 ± 0.89	0.60 ± 0.35	3.70

Table 7: Values of the objective function $\mathcal{L}_6$ and the errors $\widetilde{r}$ using the SSRVEs shown in Figure 14.

4.4 Discussion

For a concluding discussion of the optimizations and the virtual experiments in the previous subsections we summarize the results in Table 8. The values $\mathcal{L}_i$ of the corresponding objective function represent the optimization level of accuracy of the generated SSRVE. Whereas, the overall average errors $\widetilde{r}_{\varnothing}$ describe the accuracy of the virtual experiments of the SSRVEs compared with those of the target structure. At first we take a look at the overall behavior of the least-square functionals $\mathcal{L}_i$. In most of the cases we observe a decreasing value for $\mathcal{L}_i$ along with an increasing number of sampling points and therewith increasing morphology complexity. This behavior was expected, as the number of sampling points represents the degree-of-freedoms for the minimization problem during the SSRVE generation.
The improvement of the mechanical error with a decreasing value of the minimal least-square functional is observed for the objective functions, where the spectral density is taken into account and where the specific internal surface is not considered ($\mathcal{L}_3$ and $\mathcal{L}_5$). This indicates that the specific internal surface seems not to be a very suitable statistical measure. Although the specific integral of mean curvature seems not to degrade the quality of the mechanical error when using the spectral density, it does also not improve the quality particularly. This can be seen for the examined microstructures by a more or less similar behavior with respect to the mechanical response of the SSRVEs obtained from objective functions $\mathcal{L}_3$ and $\mathcal{L}_5$. Comparing the overall average errors of the first three measure combinations $\mathcal{L}_1$, $\mathcal{L}_2$ and $\mathcal{L}_3$ we notice that a suitable improvement of the mechanical error with increasing complexity of the SSRVE is only obtained for the objective function where the spectral density is taken
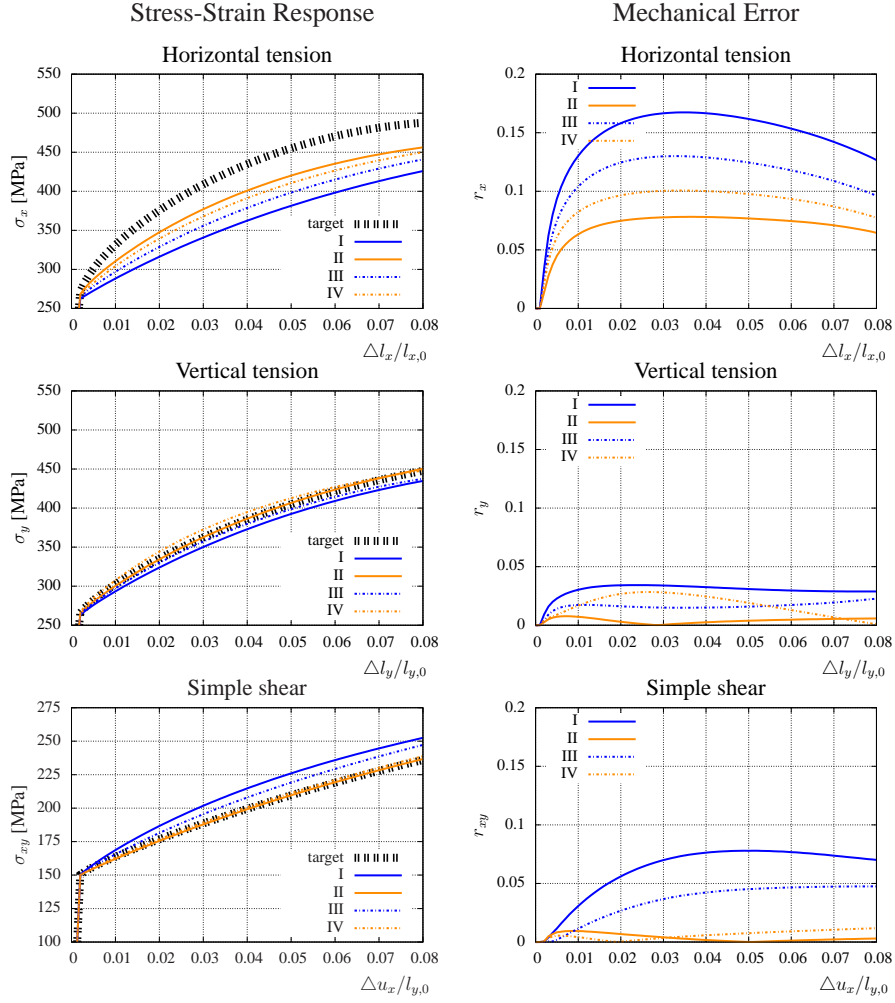
Figure 15: Results of the virtual experiments using the discretizations of the SSRVEs based on $\mathcal{L}_6$ (Figure 14).

into account ($\mathcal{L}_3$). In addition, also the absolute values of the mechanical errors besides SSRVE type I, in particular for the horizontal and vertical tension tests, are lower for $\mathcal{L}_4$. This is somehow obvious since a macroscopically anisotropic target structure is taken into account and the specific internal surface as well as the specific integral of mean curvature are not able to cover directional information.

SSRVE type	$\mathcal{L}_1$ [-]	$\widetilde{r}_\varnothing$ [%]	$\mathcal{L}_2$ [-]	$\widetilde{r}_\varnothing$ [%]	$\mathcal{L}_3$ [-]	$\widetilde{r}_\varnothing$ [%]	$\mathcal{L}_4$ [-]	$\widetilde{r}_\varnothing$ [%]	$\mathcal{L}_5$ [-]	$\widetilde{r}_\varnothing$ [%]	$\mathcal{L}_6$ [-]	$\widetilde{r}_\varnothing$ [%]
I	0.0188	4.89	0.2647	4.77	0.0144	7.34	0.0343	7.32	0.2792	4.95	0.2853	7.86
II	$1.5 \cdot 10^{-9}$	4.06	$8.5 \cdot 10^{-4}$	3.48	0.0133	3.78	0.0134	4.37	0.0142	4.44	0.0144	2.56
III	$1.5 \cdot 10^{-9}$	5.32	$8.5 \cdot 10^{-4}$	4.43	0.0127	4.97	0.0131	5.42	0.0131	4.39	0.0139	5.43
IV	$2.4 \cdot 10^{-10}$	3.40	$8.5 \cdot 10^{-4}$	4.47	0.0100	3.38	0.0132	5.94	0.0122	3.53	0.0140	3.70

Table 8: Values $\mathcal{L}_i$ of the corresponding objective functions and the overall average errors $\widetilde{r}_\varnothing$ of the virtual experiments using the SSRVEs from all minimization problems 1-6.

5 Conclusion

In this contribution the applicability of different statistical measures describing the microstructural morphology to the construction of statistically similar representative volume elements (SSRVEs) were studied. The generation of SSRVEs was based on the minimization of an ojective function considering the difference of statistical measures computed from the "real" microstructure and the SSRVE. For an estimation of the possibility of the measures to cover mechanical information of the microstructure we compared the mechanical response of virtual experiments performed for the SSRVEs with those of the target structure.

As an important overall information of the morphology the volume fraction was firstly combined pairwise with the specific internal surface, the specific integral of mean curvature and the spectral density. Then the spectral density turned out to be the most suitable parameter besides the volume fraction for the SSRVE generation and was therefore combined with each of the both others for further studies. However, no improvement was observed when extending the objective function taking into account the spectral density and the volume fraction by one of the other basic parameters. In fact, even worse results were obtained when using the specific internal surface. However, the spectral density turned out to be a suitable measure for the description of inclusion phase morphology, although further improvements are expectable by applying statistical measures of higher order as e.g. lineal-path functions or three-point probability functions. In addition to that, the parameterization of the SSRVEs by splines that are generally permitted to transform arbitrarily in the search space needs to be investigated. Probably improved results can be expected when constraining the splines such that e.g. no intersections of individual splines are allowed.

References

Balzani, D.; Schröder, J.: Some basic ideas for the reconstruction of statistically similar microstructures for multi-scale simulations. *Proceedings in Applied Mathematics and Mechanics*, 8, (2008), 10533–10534.

Balzani, D.; Schröder, J.; Brands, D.: FE^2-simulation of microheterogeneous steels based on statistically similar RVE's. In: *Proceedings of the IUTAM Symposium on Variational Concepts with applications to the mechanics of materials, September 22-26, 2008, Bochum, Germany* (2009a), in press.

Balzani, D.; Schröder, J.; Brands, D.; Carstensen, C.: Fe^2-simulations in elasto-plasticity using statistically similar representative volume elements. *Proceedings in Applied Mathematics and Mechanics*, in press.

Brekelmans, W.; Smit, R.; Meijer, H.: Prediction of the mechanical behaviour of nonlinear heterogeneous systems by multi-level finite element modelling. *Computer Methods in Applied Mechanics and Engineering*, 155, (1998), 181–192.

Conn, A. R.; Scheinberg, K.; Vicente, L. N.: *Introduction to derivative-free optimization*, vol. 8 of *MPS/SIAM Series on Optimization*. Society for Industrial and Applied Mathematics (SIAM), Philadelphia, PA (2009).

Geers, M.; Kouznetsova, V.; Brekelmans, W.: Multi-scale first-order and second-order computational homogenization of microstructures towards continua. *International Journal for Multiscale Computational Engineering*, 1, (2003), 371–386.

Hill, R.: Elastic properties of reinforced solids: some theoretical principles. *Journal of the Mechanics and Physics of Solids*, 11, (1963), 357–372.

Klinkel, S.: *Theorie und Numerik eines Volumen-Schalen-Elementes bei finiten elastischen und plastischen Verzerrungen*. Ph.D. thesis, Universität Fridericiana zu Karlsruhe (2000).

Kolda, T. G.; Lewis, R. M.; Torczon, V.: Optimization by direct search: new perspectives on some classical and modern methods. *SIAM Rev.*, 45, 3, (2003), 385–482 (electronic).

Kröner, E.: Allgemeine Kontinuumstheorie der Versetzung und Eigenspannung. *Archive of Rational Mechanics and Analysis*, 4, (1960), 273–334.

Lee, E.: Elasto-plastic deformation at finite strains. *Journal of Applied Mechanics*, 36, (1969), 1–6.

Mäkelä, M. M.; Neittaanmäki, P.: *Nonsmooth optimization*. World Scientific Publishing Co. Inc., River Edge, NJ (1992).

Miehe, C.: *Kanonische Modelle multiplikativer Elasto-Plastizität. Thermodynamische Formulierung und Numerische Implementation.*. Ph.D. thesis, Universität Hannover, Institut für Baumechanik und Numerische Mechanik, Bericht-Nr. F93/1 (1993), Habilitationsschrift.

Miehe, C.; Schröder, J.; Schotte, J.: Computational homogenization analysis in finite plasticity. simulation of texture development in polycrystalline materials. *Computer Methods in Applied Mechanics and Engineering*, 171, (1999), 387–418.

Miehe, C.; Stein, E.: A canonical model of multiplicative elasto-plasticity formulation and aspects of the numerical implementation. *European Journal of Mechanics, A/Solids*, 11, (1992), 25–43.

Nelder, J. A.; Mead, R.: A simplex method for function minimization. *The Computer Journal*, 7, (1965), 308–313.

Ohser, J.; Mücklich, F.: *Statistical analysis of microstructures in materials science*. J Wiley & Sons (2000).

Parzen, E.: *Stochastic processes*. Holden-Day, San Francisco, Calif. (1992).

Peric, D.; Owen, D.; Honnor, M.: A model for finite strain elasto-plasticity based on logarithmic strains: Computational issues. *Computer Methods in Applied Mechanics and Engineering*, 94, (1992), 35–61.

Povirk, G.: Incorporation of microstructural information into models of two-phase materials. *Acta Metallurgica*, 43/8, (1995), 3199–3206.

Schramm, H.; Zowe, J.: A version of the bundle idea for minimizing a nonsmooth function: conceptual idea, convergence analysis, numerical results. *SIAM J. Optim.*, 2, 1, (1992), 121–152.

Schröder, J.: *Homogenisierungsmethoden der nichtlinearen Kontinuumsmechanik unter Beachtung von Stabilitätsproblemen*. Ph.D. thesis, Bericht aus der Forschungsreihe des Institut für Mechanik (Bauwesen), Lehrstuhl I (2000), Habilitationsschrift.

Schröder, J.; Balzani, D.; Richter, H.; Schmitz, H.; Kessler, L.: Simulation of microheterogeneous steels based on a discrete multiscale approach. In: P. Hora, ed., *Proceedings of the 7th International Conference and Workshop on Numerical Simulation of 3D Sheet Metal Forming Processes*, pages 379–383 (2008).

Simo, J.: A framework for finite strain elastoplasticity based on maximum plastic dissipation and the multiplicative decomposition: Part i. continuum formulation. *Computer Methods in Applied Mechanics and Engineering*, 66, (1988), 199–219.

Simo, J.: Algorithms for static and dynamic multiplicative plasticity that preserve the classical return mapping schemes of the infinitesimal theory. *Computer Methods in Applied Mechanics and Engineering*, 99, (1992), 61–112.

Simo, J.; Miehe, C.: Associative coupled thermoplasticity at finite strains: Formulation, numerical analysis and implementation. *Computer Methods in Applied Mechanics and Engineering*, 96, (1992), 133–171.

Smit, R.; Brekelmans, W.; Meijer, H.: Prediction of the mechanical behavior of nonlinear heterogeneous systems by multi-level finite element modeling. *Computer Methods in Applied Mechanics and Engineering*, 155, (1998), 181–192.

Weber, G.; Anand, L.: Finite deformation constitutive equations and a time integration procedure for isotropic, hyperelastic-viscoelastic solids. *Computer Methods in Applied Mechanics and Engineering*, 79, (1990), 173–202.

Addresses: Dr.-Ing. Daniel Balzani, Institute of Mechanics and Computational Mechanics, Leibniz University Hannover, D-30167 Hannover.
email: daniel.balzani@ibnm.uni-hannover.de.
Dominik Brands, Jörg Schröder, Institute of Mechanics, University of Duisburg-Essen, D-45117 Essen.
email: dominik.brands@uni-due.de, j.schroeder@uni-due.de
Carsten Carstensen, Institute of Mathematics, Humboldt-University Berlin, D-10099 Berlin.
email: cc@math.hu-berlin.de